Self-healing of broken bonds and deep gap states in Sb_2Se_3 and Sb_2S_3

*Keith Patrick McKenna**

Prof. Keith Patrick McKenna
Department of Physics, University of York, Heslington, York YO10 5DD, United Kingdom.
Email Address: keith.mckenna@york.ac.uk

Keywords: *Chalcogenides, surface defects, gap states, density functional theory*

Broken bonds introduced at extended defects in covalently-bonded semiconductors generally introduce deep electronic states within the gap, negatively impacting performance for applications in electronics, photochemistry and optoelectronics. Here it is shown that Sb_2Se_3 and Sb_2S_3, which are showing exceptional promise for photovoltaic and photoelectrochemical applications, exhibit a remarkable ability to self-heal broken bonds through structural reconstructions, thereby eliminating the associated deep electronic states. Unusually, these materials appear intrinsically resilient to the formation of dangling bonds at extended defects which should be advantageous for wide ranging applications. This novel behaviour is connected with particular structural and chemical features of Sb_2Se_3 and Sb_2S_3 and a number of other materials that may be expected to exhibit similar effects are identified.

1 Introduction

Antimony selenide (Sb_2Se_3) along with the related sulfide and selenosulfide phases are emerging as very promising materials for thin film photovoltaic (PV) and photoelectrochemical applications.[1–7] They are stable, earth abundant, non-toxic and exhibit strong optical absorption with band gaps in the optimal range for harvesting solar energy.[8] Furthermore, the band gap and film morphology can be tuned by anion mixing with antimony selenosulfide solar cells very recently reaching a certified efficiency of 10%.[7] These high efficiencies reached in a relatively short period of time have been suggested to be connected to the unique structure of Sb_2Se_3, which involves one-dimensional (1D) $(Sb_4Se_6)_n$ ribbons oriented along the [001] direction (Pbnm space group).[1,5,9] The expectation is that extended defects (such as grain boundaries) will form more easily between the ribbons — due to the weaker nature of the inter-ribbon bonds (with significant Van der Waals character) — hence they should only weakly perturb electronic properties. However, Sb_2Se_3 thin films grow with preferential (211) or (221) texture meaning that the ribbons are inclined with respect to the substrate.[3,4,9] Therefore, the presence of dangling bonds due to termination of ribbons at extended defects would seem inevitable in polycrystalline films. Indeed, such grain boundaries have recently been observed directly in Sb_2Se_3 by aberration-corrected scanning transmission electron microscopy.[10] Since dangling bonds usually introduce deep levels inside the band gap of semiconductors, leading to non-radiative recombination and loss of performance, it would seem on first sight that the particular structure of Sb_2Se_3 should not convey any special grain boundary tolerance. The impact of such dangling bond defects on performance of CdTe PV devices, for example, is well appreciated and post-deposition treatment with metal chlorides has proved essential to achieve acceptable performance.[11–13] However, unexpectedly initial density functional theory (DFT) calculations suggest that at least some extended defects involving broken ribbons do not present problematic deep states in the gap either.[10] The origin and generality of this effect is a key open question.

Here, we present a computational study of the structure, relaxation and electronic properties of a series of low- and high-index surfaces in Sb_2Se_3 and Sb_2S_3, each of which involve perturbation of the 1D ribbon structure to different degrees. Our DFT calculations employ the HSE06 hybrid functional together the DFT-D3 correction method of Grimme for description of dispersion interactions[14,15] (hereafter HSE+D3, see Methods for details) that has previously been applied successfully to model intrinsic point defects in Sb_2Se_3.[16] Such calculations are computationally expensive for the types of system we consider here (with supercells containing well over one hundred atoms) but is important for accurate prediction of structure and electronic properties. We find that for all surfaces that have 1D ribbons oriented at an angle to the surface, the breaking of bonds leads to deep states in the gap. The surface formation energies of the initially cleaved surfaces (before relaxation) are found to correlate with the number of broken intra-ribbon bonds. However, following a full geometry optimisation there is significant relaxation with formation energies are reduced by more than 50% . Importantly, the undercoordinated surface atoms relax to form new inter- and intra-ribbons bonds in such as way as to maintain bulklike coordination of all atoms at the surface. Correlated with these significant surface reconstruction, the deep states within the band gap are removed. Similar effects have been observed previously for the (110) surfaces of III-V semiconductors,[17] but what is more extraordinary here is that the surface reconstructions seem to be effective for all surface terminations considered. Very similar results are found for the sulfide phase, which has slightly higher surface formation energies owing to the smaller unit cell volume (hence reduced density of broken intra-ribbon bonds). These results suggest that surfaces in Sb_2Se_3 and Sb_2S_3 have an intrinsic ability to self heal, removing deep dangling bond states from the gap, due to a remarkable flexibility in the structure allowing broken intra-ribbon bonds to be healed by formation of new inter- and inter-ribbon bonds. We discuss the origins of this effect from a materials perspective and suggest other materials that may display similar effects.

2 Results

Sb_2Se_3 and Sb_2S_3 are sesqui-chalcogenides with the stibnite crystal structure (space group Pnma, or equivalently Pbnm). For the band structures and surfaces that follow we adopt the Pbnm setting (which differs from Pnma only by a rotation) to be consistent with previous literature. The crystal structure involves 1D ribbons of $(Sb_4[Se/S]_6)_n$ oriented along the [001] direction (**Figure 1**). The experimentally determined lattice constants for Sb_2Se_3 are a = 11.6288 Å, b = 11.7758 Å and c = 3.9763 Å[18] and for Sb_2S_3 are a = 11.3107 Å b = 11.2285 Å and c = 3.8363 Å.[19] At the HSE+D3 level of theory the calculated lattice constants, a = 11.51984 Å, b = 11.91167 Å and c = 3.97574 Å (Sb_2Se_3) and a = 11.38577 Å, b = 11.20971 Å and c = 3.79893 Å (Sb_2S_3), are in very good agreement with experiment (within around 1 %). The band gaps predicted at the HSE+D3 level of theory (Figure 1) for both Sb_2Se_3 and Sb_2S_3 (1.4 and 2.1 eV) are also in reasonable agreement with experiment (1.2 eV and 1.7 eV) albeit slightly overestimated.[18,20–22]

To help analyse and interpret the structural and electronic perturbations induced by surfaces in Sb_2Se_3 and Sb_2S_3 it is useful to have a quantitative means to describe the undercoordination of atoms induced by surfaces (bond breaking). However, the definition of coordination in these materials is not straightforward as there is a mixture of short strong bonds as well as longer weaker bonds with significant (but not entirely) Van der Waals

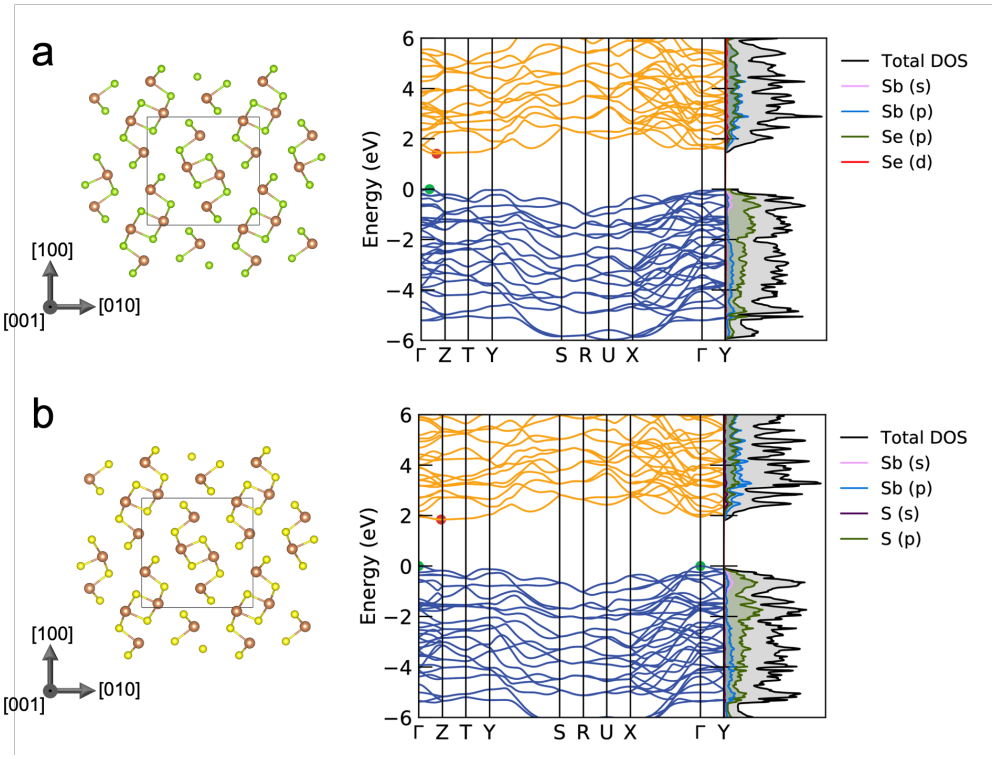

Figure 1: Structure, band structure and density of states of (a) Sb_2Se_3 and (b) Sb_2S_3 calculated using the HSE+D3 method. Sb atoms are depicted as brown spheres and Se atoms by green spheres in this and subsequent figures.

Table 1: Calculated surface formation energies (E_f) for the (010), (001), (041) and (273) surfaces of Sb_2Se_3 and Sb_2S_3. Formation energies are determined for the unlrelaxed (unrel) and the fully optimised (rel) surface structures and the difference (Δ) is also shown. The number of broken bonds per unit area ($\Delta Z/A$) for the as cleaved surfaces are also given in the Table.

		PBE+D3 (Jm^{-2})			HSE+D3 (Jm^{-2})		
	$\Delta Z/A$ (nm^{-2})	E_f (unrel)	E_f (rel)	Δ	E_f (unrel)	E_f (rel)	Δ
Sb_2Se_3							
(010)	0.0	0.36	0.23	0.13	0.27	0.25	0.02
(001)	8.7	0.76	0.42	0.34	0.83	0.42	0.41
(041)	8.7	0.99	0.46	0.53	1.10	0.48	0.63
(273)	8.7	0.96	0.48	0.48	-	-	-
Sb_2S_3							
(010)	0.0	0.44	0.24	0.20	0.27	0.25	0.02
(001)	9.4	0.87	0.40	0.47	0.92	0.35	0.57
(041)	9.4	1.16	0.51	0.65	1.27	0.50	0.77
(273)	9.3	1.13	0.48	0.65	-	-	-

character.[23] For example, taking the HSE+D3 optimized structure of Sb_2Se_3 one can identify two Sb sites. Sb(1) has 6 neighboring Se sites at distances $d = \{2.658, 2.670, 2.670, 3.188, 3.188, 3.216\}$ Å. The closest 5 Se are in the same 1D ribbon as the Sb (hence they form intra-ribbon bonds) while the most distant form an inter-ribbon bond. Sb(2) has 7 neighboring Se sites at $d = \{2.592, 2.786, 2.975, 2.975, 2.975, 3.517, 3.517\}$ Å. The closest 5 form intra-ribbon bonds while the two most distant form inter-ribbon bonds. For Sb_2Se_3 in the analysis below we take $d < 3.0$ Å as the definition of a bond (thereby focusing on the strongest bonds that are likely to have the most significant effect on electronic properties when broken). In this case for the ideal bulk Sb_2Se_3 crystal we define Sb(1) as 3-coordinated, Sb(2) as 5-coordinated and Se sites as 2- or 3-coordinated (with all bonds intra-ribbon). The corresponding site distances for Sb_2S_3 are for Sb(1) $d = \{2.493, 2.515, 2.515, 3.110, 3.110, 3.179\}$ and for Sb(2) $d = \{2.439, 2.652, 2.652, 2.811, 2.811, 3.415, 3.415\}$. Notably the length of the inter-ribbon bonds in Sb_2S_3 are very similar to those in Sb_2Se_3 (about 2% shorter) while the intra-ribbon bonds are around 6% shorter. For the analysis of coordination in Sb_2S_3 we therefore use a correspondingly reduced cut-off of $d < 2.9$ Å. While one could employ more advanced approaches to analyse bonding the usefulness of this simple definition is demonstrated below in its ability to act as a simple semi-quantitative predictor of surface formation energy and perturbation of the electronic structure. Since very similar results are obtained for the structure and relaxation of Sb_2Se_3 and Sb_2S_3 we focus the presentation of results on Sb_2Se_3 but summarise all results in **Table 1** and provide all structures in the Supporting Information.

First we consider the (010) which has the 1D ribbons oriented parallel to the surface. Since no intra-ribbon bonds are broken when cleaving the bulk crystal it is anticipated the surface formation energy will be relatively low and that the perturbation of the electronic structure will be minimal. Therefore, this surface provides a useful reference for the more perturbing surface orientations that will follow. Indeed, we find that the HSE+D3 computed surface formation energy (SFE) is 0.25 Jm^{-2}. The difference between the unrelaxed SFE (i.e. the formation energy of the as-cleaved surface) and the fully optimized surface (Δ) is a useful measure of the degree of relaxation. For this surface Δ is extremely small (0.02 Jm^{-2}) reflecting the very small distortion in structure near the surface (**Figure 2a-**

b).
We next consider the (001) surface which has the 1D ribbons oriented perpendicular to the surface. As a consequence the coordination of all atoms in the outermost layers are reduced relative to the bulk. Most significantly the coordination of two surface Se atoms on each surface are reduced to 1 and the coordination of two surface Sb atoms are reduced to 2 (both lower than the minimum coordinations found in the bulk crystal). Correlated with this significant disruption the unrelaxed SFE is found to be much higher than that of the (010) surface: 0.83 Jm^{-2}. However, there is a significant reconstruction of the surface following structural optimisation (**Figure 2c-d**, **Figure S1**). The 2-coordinated surface Sb atoms distort shortening one of the longer intra-ribbon bonds from 3.188 Å to 2.652 Å and thereby increasing their coordination from 2 to 3. Surface Sb atoms distort to form strong inter-ribbon bonds ($d = 2.647$ Å) with the under-coordinated surface Se atoms raising their coordination from 1 to 2. By forming these bonds the coordination of the Sb site is reduced (from 5 to 3) and neighboring Se are also reduced in coordination from (3 to 2). However, after this surface reconstruction all Se have coordination of at least 2 and all Sb at least 3 (i.e. the same minimum coordinations found in the bulk). In the outermost two layers (within 2 Å of the surface) there are significant changes in bonds lengths even for sites that do not change their coordination (up to 10%). There is also considerable distortion of bonds due to strain propagating below surface reflected in a significantly lower relaxed SFE ($\Delta = 0.41$ Jm^{-2}). For the (001) surface where the ribbons are aligned perpendicular to surface the number of surface atoms can be defined fairly unambiguously (i.e. all atoms within the outermost layers). In this case one can calculate the formation energy in terms of the excess energy per surface atom which for Sb_2Se_3(001) is 0.26 eV per surface atom and for Sb_2S_3(001) is 0.28 eV per surface atom (at the HSE+D3 level). However, for the other surfaces considered in this manuscript defining the number of surface atoms is less straightforward.
The (041) surface has the 1D ribbons oriented at an angle to the surface normal (**Figure 3a**) and is associated with a very similar number of bonds per unit area (Table 1). As a result the unrelaxed SFE is again large (1.10 Jm^{-2}). However, on structural optimization there is considerable reconstruction with formation of new intra- as well inter-ribbon bonds (**Figure 3b**) as well significant changes in bond lengths. Once again, the net result is that there are no atoms in the surface with coordination lower than the minimum coordinations found in the bulk. This is reflected in a significantly lower relaxed SFE of 0.48 Jm^{-2}, very similar to the relaxed SFE for the (001) surface.
Finally, we consider the (273) surface which again has the 1D ribbons inclined at an angle to the surface normal (**Figure 3c-f**). The supercell required to model this surface is very large (400 atoms) and so it is not feasible to perform the structural optimization at the HSE+D3 level. However, we note for all the surfaces considered above the atomic structures and formation energies calculated the the PBE+D3 level are very consistent with the HSE+D3 results (Table 1) therefore we will employ PBE+D3 alone for this surface. The density of broken bonds for this surface is again very similar to the previous surfaces that involve tuncation of the 1D ribbons (Table 1) and as a result the unrelaxed SFE is found to be rather similar (0.96 Jm^{-2}). One again the reconstruction following geometry optimization involves formation of new intra- and inter-ribbons bonds as well as significant changes in bond lengths. The net result is that almost all atoms in the surface have coordination equal or greater than the minimum coordinations found in the bulk. The one

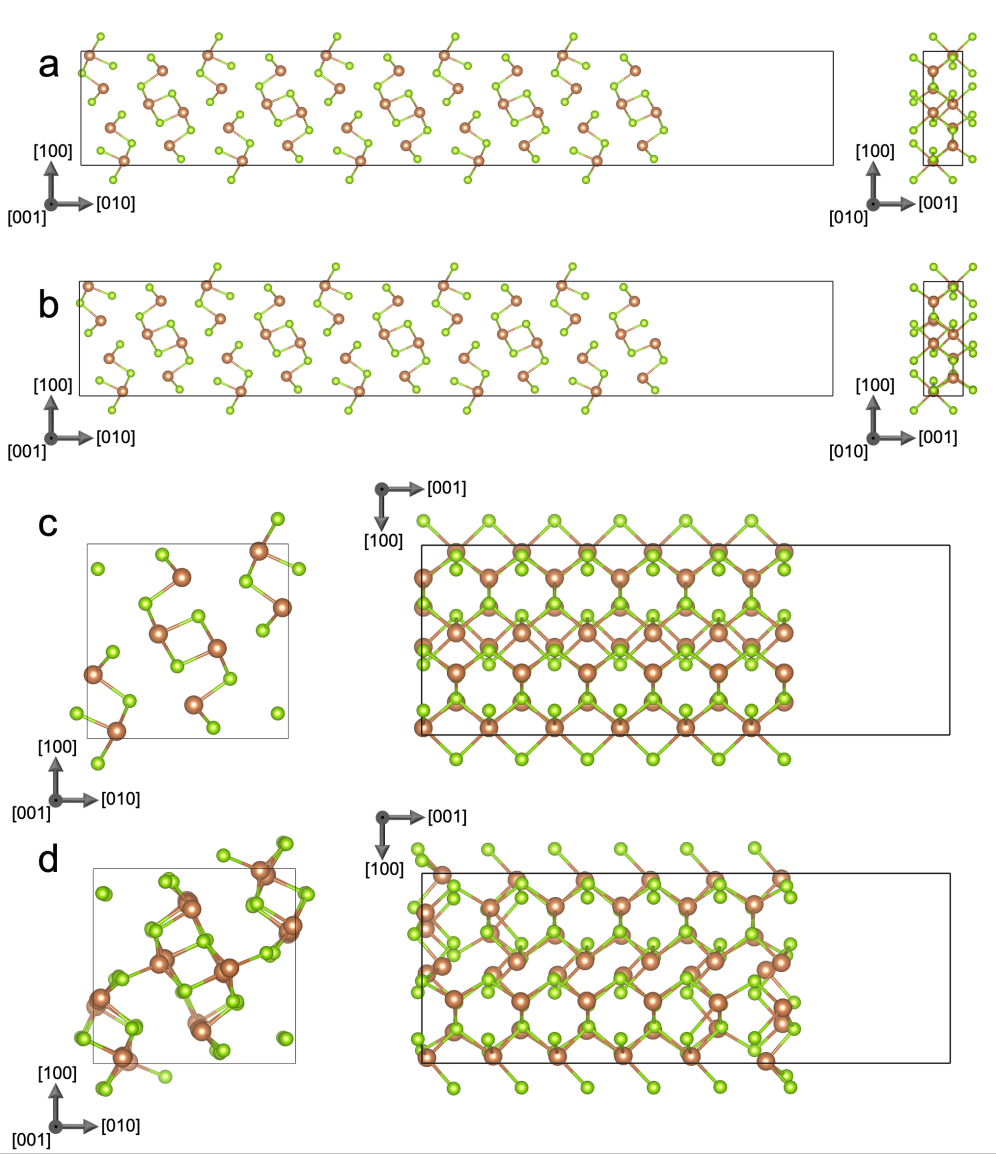

Figure 2: Structures of the Sb_2Se_3(010) surface (a) before and (b) after structural optimization and the Sb_2Se_3(001) surface (c) before and (d) after structural optimization.

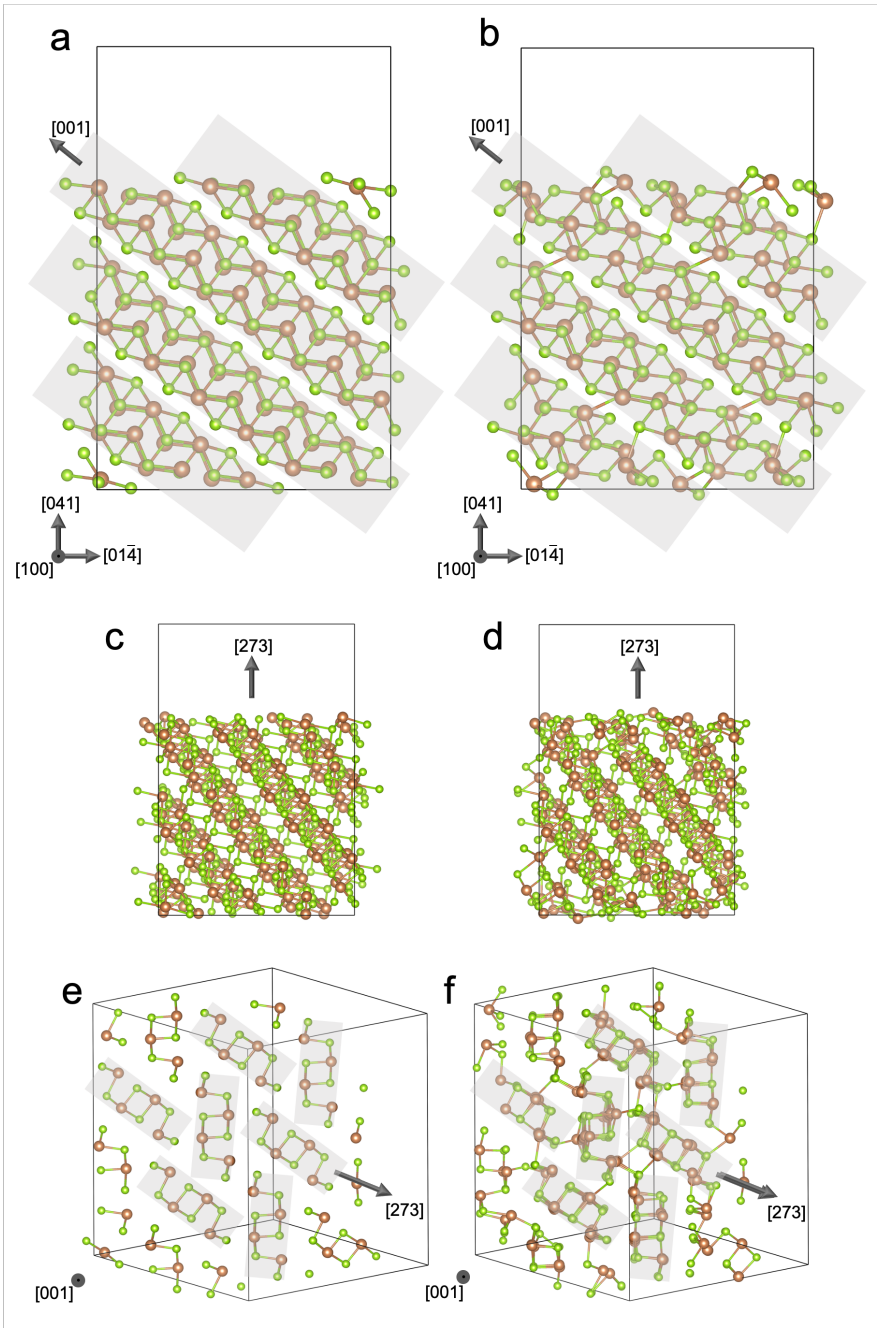

Figure 3: Structure of the Sb_2Se_3(041) surface (a) before and (b) after structural optimisation using HSE+D3. Structure of the Sb_2Se_3(273) surface (c) before and (d) after structural optimisation using PBE+D3. Alternative views oriented along the length of the Sb_2Se_3 ribbons are shown in (e) before relaxation and (f) after relaxation. The Sb_2Se_3 ribbons are highlighted by the shaded areas.

exception is two Se sites on each surface that strictly according to our chosen definition has a coordination of 1. This significant relaxation is reflected in the fact the relaxed SFE (0.48 Jm^{-2}) is again comparable to the other surfaces that disrupt the 1D ribbons.
We find very similar trends for Sb_2S_3 (see Table 1), however SFE are slightly higher in Sb_2S_3 consistent with the reduced area and therefore increased density of broken bonds. Both materials demonstrate a remarkable ability to easily form new intra- and inter-ribbon bonds to compensate for broken bonds at the surface and restore atom coordinations to bulklike values. This is reflected in surprisingly low relaxed SFEs for any surface that leads to the cleavage of 1D ribbons (around 0.4-0.5 Jm^{-2}). This is only slightly larger that the SFE for the (010) surface that has the 1D ribbons running parallel to the surface (0.25 Jm^{-2}) and exhibits almost no relaxation on cleavage.

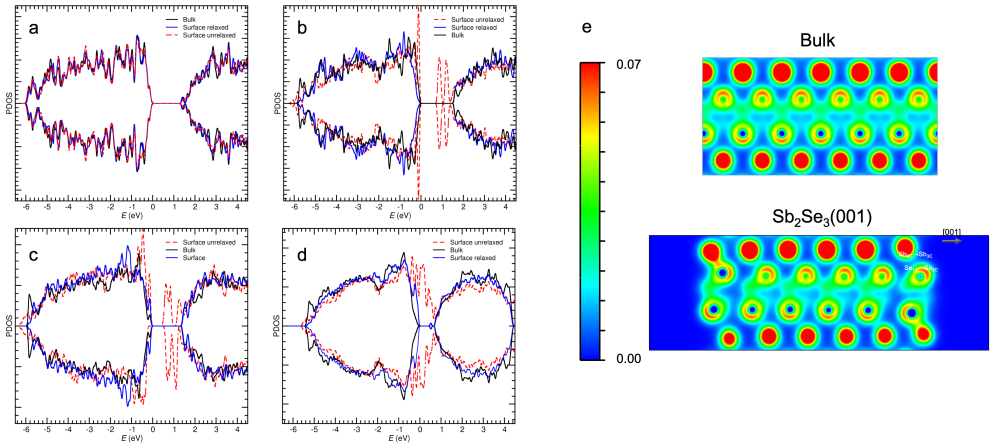

Figure 4: Electronic density of states projected onto the bulk-regions of the surface slabs (bulk), the surface regions of the unlrelaxed surface slabs (surface unrelaxed) and the surface regions of the relaxed surface (surface relaxed). (a) Sb_2Se_3(010), (b) Sb_2Se_3(001), (c) Sb_2Se_3(041) and (d) Sb_2Se_3(273). (e) Cross-section of the electron density on a (100) plane cutting through the Sb(2) surface site for bulk crystal and the reconstructed Sb_2Se_3(001) surface.

We now turn to the electronic properties of surfaces in Sb_2Se_3. In the following we will present and discuss electronic densities of states for both the unrelaxed (as cleaved) and relaxed surfaces and in each case we will show projected densities of states (PDOS) for the surface and bulk regions of the slabs (details of the regions used for projections are given in the Supporting Information together with PDOS figures for Sb_2S_3, **Figure S2**). Note that all calculations are performed including spin-polarization so as not to bias the optimization unduly and all PDOS figures are therefore shown for both spin channels. However, for all but one of the surfaces the predicted electronic ground state is predicted to be non-spin-polarized. For the (010) surface (**Figure 4a**) we see that the surface PDOS for the unrelaxed surface is almost identical to that of the relaxed surface and gives rise to no states in the gap. This is consistent with the very small SFE and the fact that no bonds and broken and is in line with previous reports. However, as anticipated the unrelaxed (001), (041) and (273) surfaces all present significant gap states due to broken bonds (Figure 4). These gap states have mixed Se- and Sb-*p* character (**Figure S3** and **Figure S4** in Supporting Information). Band decomposed charge densities for individual states in the gap of the unrelaxed surfaces show they have primarily Se-*p* and Sb-*p* character and are associated with undercoordinated atoms near the surface. (**Figure S5**, **Figure S6** and

Figure S7 in Supporting Information). For the (273) these gap states are so significant the surface essentially becomes metallic. However, for all three surfaces on relaxation the gap states are almost entirely eliminated. Even shallow states appear to be absent. There is a small feature in the PDOS for the (273) surface but this is also found in the bulk region and is an small artefact due to the finite slab thickness. The degree to which these results are unexpected should not be understated. Some surfaces in some materials show an ability to heal broken bonds and leave the gap largely free of deep gap states. However, it is unprecedented to find materials that can so-effectively heal broken bonds (for a wide range of surfaces) and remove almost all traces of surface-related gap states.
To provide some insight into the possible role of the Sb lone pair on surface reconstruction we also analyse the total electron density for the Sb_2Se_3(001) surface. **Figure 4e** shows a cross-sections of the electron density through a (100) plane passing through the Sb(2) surface site. For reference we first show the electron density for a bulk supercell with the same dimensions and orientation as the surface supercell. The lone pairs on Sb can be recognised by the crescent-like features and in the bulk crystal project into the gaps between the 1D ribbons. For the (001) surface the distortion of the five-coordinated Sb atom to form a bond with the one-coordinated Se atom is apparent involving a significant reorientation of the lone pair so that it projects towards the centre of the slab. The lone pair on the two-coordinated Sb atom is also slightly reoriented as are those on other Sb atoms deeper into the slab reflecting long strain that propegates far from the surface. Analysis of the orbital-projected DOS (**Figure S3** and **Figure S4** in Supporting Information) shows that in the bulk the Sb *s*-states involved in the lone pair mainly fall in a region within around 1 eV of the valence band maximum. For the unrelaxed (001) surface there is a notable broadening of these states and a more localized feature at the valence band maximum. However, following optimization the Sb *s*-projected DOS is very similar to the bulk.

3 Discussion and Conclusions

In order to fully appreciate the uniqueness of the self-healing behavior observed for Sb_2Se_3 and Sb_2S_3 it is useful to review what is known about the surface structure and electronic properties of other compound semiconductors. In particular, surfaces of GaAs surfaces have been the focus on many previous studies driven by both fundamental interest and applications of GaAs-based devices. First principles calculations predict the unrelaxed GaAs(110) surface exhibits surface states related to anion and cation dangling bonds deep within the bulk band gap.[24,25] The relaxation of this surface involves a bond-length-conserving rotation relaxation in which the cation relaxed outwards and the anion inwards (with maximum atom displacements of around 0.3-0.4 Å). Although this represents a significant relaxation we note it is not as dramatic as the intra-ribbon bond forming relaxations observed for Sb_2Se_3 and Sb_2S_3 (with many atoms within 5 Å of the surface exhibiting displacements larger than 0.3 Å and maximum atom displacements of up to 1.4 Å). Associated with this relaxation the anion-related gap states are moved below the valence band maximum and the cation-related gap states move to just below the conduction band minimum. Therefore, the gap is largely (but not completely as in the case of Sb_2Se_3 and Sb_2S_3) cleared of gap states. These predictions are consistent with experimental data from low-energy electron-diffraction analyses, scanning tunnelling microscopy, photoemission and inverse-photoemission.[17,24,26] The (110) surfaces in structurally similar materials such

as GaP, InP, InAs and β-SiC undergo a similar relaxation however deeper gap states remain.[24,25] The GaAs(001) surface has various proposed reconstructions, many of which are As-rich. First principles calculations predict most of these surfaces exhibit gap states even after reconstruction although in the case of the β2(2x4) reconstructions these are rather shallow.[27] Likewise GaAs(111) surfaces also predicted to exhibit significant gap states and various schemes for pasivation (such as with S or Se).[28]

The results above demonstrate that Sb_2Se_3 and Sb_2S_3 are able to readily heal broken bonds at surfaces that would otherwise give rise to deep states within their band gaps. For applications in photovoltaics and photoelectrochemistry this is highly beneficial as it should make them intrinsically resilient to the harmful effects of broken bonds at extended defects such as increased recombination and open circuit voltage deficit. In many ways Sb_2Se_3 and Sb_2S_3 could be considered as the salamander of the materials world; since they too demonstrate the impressive ability to self-repair when cleaved. The natural question that arises is why these particular materials exhibit this effect when so many others do not. What is it in the DNA of these materials that activates this trait and could it be found in other materials?

Analysis of the surface reconstructions suggests a key feature is the coordination environment of Sb sites which involve a number of short (strong) intra-ribbon bonds as well as longer (weak) intra- and inter-ribbon bonds. When short bonds are broken the structure can distort to replace them by shortening the distance of one of the (previously) long bonds. The presence of lone pair electrons on Sb, which increases the flexibility of bond angles and reduces strain energy, is also likely an important factor in explaining the ability to readily reconfigure in response to cleaved bonds. However, one should be cautious about viewing this as a feature of the cation alone since the electronic properties of lone-pair cations cannot be fully separated from the anion.[29] Furthermore, the 1D ribbon structure with more open spaces between is also likely to help reduce strain energies associated with the necessary distortions compared to a three-dimensional covalently bonded material. All these features come together in Sb_2Se_3 and Sb_2S_3 to enable the observed self-healing.

The above characteristics are most probably not unique to these materials. In fact, recent experimental and theoretical work suggests that many chalcogenides exhibit similar bonding features. The term "metavalent" has been coined to indicate bonding that is somewhere between metallic and covalent.[23] Striking differences in bond rupture processes in chalcogenides compared to conventional metallic, ionic, and covalently bonded materials have also been revealed by atom probe tomography providing support for this idea.[30] Quantum chemical calculations have shown that strong metavalent character is correlated with other unusual properties (in particular large Born effective charges, high optical dielectric constants, low Debye temperatures and large lattice anharmonicity).[31] Sb_2Se_3 and Sb_2S_3 fall into this class as well as a number of other chalcogenides such as $AgBiSe_2$, $AgBiTe_2$, $AgSbTe_2$ and SnTe. Beyond chalcogenides, given the vast configuration space of possible materials there are bound to be many other materials that exhibit self-healing raising the tantalising prospect of engineering materials that are electronically resiliant to extended defects for wide ranging applications in electronics, photochemistry, optoelectronics and energy materials.

4 Computational Methods

Spin polarised density functional theory calculations were carried out using the projector augmented wave method and a plane wave basis as implemented in the Vienna Ab initio Simulation Package (VASP).[32,33] We employ the HSE06 hybrid functional[14] together with the D3 Grimme dispersion correction to describe the Van der Waals interactions between the ribbons.[15] This approach has recently been applied to model intrinsic point defects in Sb_2Se_3.[16] The bulk crystal was optimized using a 350 eV plane wave cut off and a 2×2×6 gamma-centered k-point grid for Brillouin zone sampling. The density of states were calculated using an increased k-point sampling grid of 4×4×12. The Sumo python package used to determine the paths in reciprocal space for the band structure plots and also to produce some of the figures in this manuscript.[34] Surface supercells were constructed based on the optimized structure at the HSE+D3 level and include a vacuum gap of at least 10 Å (see Supporting Information for full details). All surfaces are first optimized at the PBE+D3 level (including spin polarization) with lattice constants fixed to values appropriate for HSE+D3 until all forces are less than 0.05 eVÅ^{-1} and then re-optimized at the HSE+D3 level. Using this approach the possibility of more stable reconstructions that could be separated from the local minima we identify by an energy barrier cannot be excluded. For the initially cleaved (unrelaxed) and fully relaxed surface structures the surface formation energy is calculated as,

$$E_{\mathrm{f}} = \frac{E_{\mathrm{surf}} - E_{\mathrm{bulk}}}{2A},$$

where E_{surf} is the total energy of the surface supercell, E_{bulk} is the total energy of a bulk supercell of the same dimensions as the surface supercell (identical settings such as k-point sampling are employed for consistency) and A is the cross-sectional area of each surface in the supercell. All surface structures and cross-sections of the charge density were visualized using the VESTA package.[35]

Supporting Information
Supporting Information available: Alternative view of the structural relaxation of the Sb_2Se_3 (001) surface, information on the surface supercells employed, electronic properties of Sb_2S_3 surfaces, orbital projected densities of states, band decomposed charge densities and VASP POSCAR structure files for all supercells. Supporting Information is available from the Wiley Online Library or from the author.

Acknowledgements
KPM would like thank Prof. Tim Veal and Drs. Jon Major and Budhika Mendis for helpful discussions and acknowledges support from the EPSRC (EP/P023843/1). This work made use of the facilities of Archer, the UK's national high-performance computing service, via our membership in the UK HPC Materials Chemistry Consortium, which is funded by the EPSRC (EP/L000202, EP/R029431) and the Viking Cluster, which is a high-performance computer facility provided by the University of York. All data relating to the density functional theory calculations created during this research are available on request from the University of York Research database (https://doi.org/TBC).

References

[1] K. Zeng, D.-J. Xue, J. Tang, *Semicond. Sci. Technol.* **2016**, *31*, 6 063001.

[2] X. Wen, C. Chen, S. Lu, K. Li, R. Kondrotas, Y. Zhao, W. Chen, L. Gao, C. Wang, J. Zhang, G. Niu, J. Tang, *Nat. Commun.* **2018**, *9*, 1 2179.

[3] O. S. Hutter, L. J. Phillips, K. Durose, J. D. Major, *Sol. Energy Mater. Sol. Cells* **2018**, *188* 177 .

[4] Z. Li, X. Liang, G. Li, H. Liu, H. Zhang, J. Guo, J. Chen, K. Shen, X. San, W. Yu, R. E. I. Schropp, Y. Mai, *Nat. Commun.* **2019**, *10*, 1 125.

[5] W. Yang, J. Ahn, Y. Oh, J. Tan, H. Lee, J. Park, H.-C. Kwon, J. Kim, W. Jo, J. Kim, J. Moon, *Adv. Energy Mater.* **2018**, *8*, 14 1702888.

[6] W. Yang, J. H. Kim, O. S. Hutter, L. J. Phillips, J. Tan, J. Park, H. Lee, J. D. Major, J. S. Lee, J. Moon, *Nat. Commun.* **2020**, *11*, 1 861.

[7] R. Tang, X. Wang, W. Lian, J. Huang, Q. Wei, M. Huang, Y. Yin, C. Jiang, S. Yang, G. Xing, S. Chen, C. Zhu, X. Hao, M. A. Green, T. Chen, *Nature Energy* **2020**.

[8] C. Chen, W. Li, Y. Zhou, C. Chen, M. Luo, X. Liu, K. Zeng, B. Yang, C. Zhang, J. Han, J. Tang, *Appl. Phys. Lett.* **2015**, *107*, 4 043905.

[9] Y. Zhou, L. Wang, S. Chen, S. Qin, X. Liu, J. Chen, D.-J. Xue, M. Luo, Y. Cao, Y. Cheng, E. H. Sargent, J. Tang, *Nat. Photonics* **2015**, *9*, 6 409.

[10] R. E. Williams, Q. M. Ramasse, K. P. McKenna, L. J. Phillips, P. J. Yates, O. S. Hutter, K. Durose, J. D. Major, B. G. Mendis, *ACS Appl. Mater. Interfaces* **2020**, *12*, 19 21730.

[11] J. D. Major, R. E. Treharne, L. J. Phillips, K. Durose, *Nature* **2014**, *511*, 7509 334.

[12] J. M. Burst, J. N. Duenow, D. S. Albin, E. Colegrove, M. O. Reese, J. A. Aguiar, C. S. Jiang, M. K. Patel, M. M. Al-Jassim, D. Kuciauskas, S. Swain, T. Ablekim, K. G. Lynn, W. K. Metzger, *Nature Energy* **2016**, *1*, 3 16015.

[13] C.-J. Tong, K. P. McKenna, *J. Phys. Chem. C* **2019**, *123*, 39 23882.

[14] A. V. Krukau, G. E. Scuseria, J. P. Perdew, A. Savin, *J. Chem. Phys.* **2008**, *129*, 12 124103.

[15] S. Grimme, *J. Comput. Chem.* **2004**, *25*, 12 1463.

[16] C. N. Savory, D. O. Scanlon, *J. Mater. Chem. A* **2019**, *7*, 17 10739.

[17] J. van Laar, A. Huijser, T. L. van Rooy, *J. Vac. Sci. Technol.* **1977**, *14*, 4 894.

[18] M. Birkett, W. M. Linhart, J. Stoner, L. J. Phillips, K. Durose, J. Alaria, J. D. Major, R. Kudrawiec, T. D. Veal, *APL Mater.* **2018**, *6*, 8 84901.

[19] P. Bayliss, W. Nowacki, *Z. Kristallogr. Cryst. Mater.* **1972**, *135*, 3-4 308 .

[20] A. Vedeshwar, *J. Phys. III* **1995**, *5* 1161.

[21] T. Fujita, K. Kurita, K. Takiyama, T. Oda, *J. Phys. Soc. Jpn.* **1987**, *56*, 10 3734.

[22] M. Y. Versavel, J. A. Haber, *Thin Solid Films* **2007**, *515*, 18 7171 .

[23] Y. Cheng, O. Cojocaru-Mirédin, J. Keutgen, Y. Yu, M. Küpers, M. Schumacher, P. Golub, J.-Y. Raty, R. Dronskowski, M. Wuttig, *Adv. Mater.* **2019**, *31*, 43 1904316.

[24] J. L. A. Alves, J. Hebenstreit, M. Scheffler, *Phys. Rev. B* **1991**, *44* 6188.

[25] M. Sabisch, P. Krüger, J. Pollmann, *Phys. Rev. B* **1995**, *51* 13367.

[26] B. Engels, P. Richard, K. Schroeder, S. Blügel, P. Ebert, K. Urban, *Phys. Rev. B* **1998**, *58* 7799.

[27] W. G. Schmidt, F. Bechstedt, *Phys. Rev. B* **1996**, *54* 16742.

[28] A. Ohtake, S. Goto, J. Nakamura, *Sci. Rep.* **2018**, *8*, 1 1220.

[29] R. G. Egdell, A. Walsh, G. W. Watson, J. Guo, P. A. Glans, T. Learmonth, K. E. Smith, *Phys. Rev. Lett.* **2006**, *96*, 15 157403.

[30] M. Zhu, O. Cojocaru-Mirédin, A. M. Mio, J. Keutgen, M. Küpers, Y. Yu, J.-Y. Cho, R. Dronskowski, M. Wuttig, *Adv. Mater.* **2018**, *30*, 18 1706735.

[31] J.-Y. Raty, M. Schumacher, P. Golub, V. L. Deringer, C. Gatti, M. Wuttig, *Adv. Mater.* **2019**, *31*, 3 1806280.

[32] G. Kresse, J. Furthmüller, *Computational Mater. Sci.* **1996**, *6*, 1 15.

[33] G. Kresse, J. Furthmüller, *Phys. Rev. B* **1996**, *54*, 16 11169.

[34] A. M. Ganose, A. J. Jackson, D. O. Scanlon, *Journal of Open Source Software* **2018**, *3*, 28 717.

[35] K. Momma, F. Izumi, *J. Appl. Crystallogr.* **2011**, *44*, 6 1272.

Table of Contents

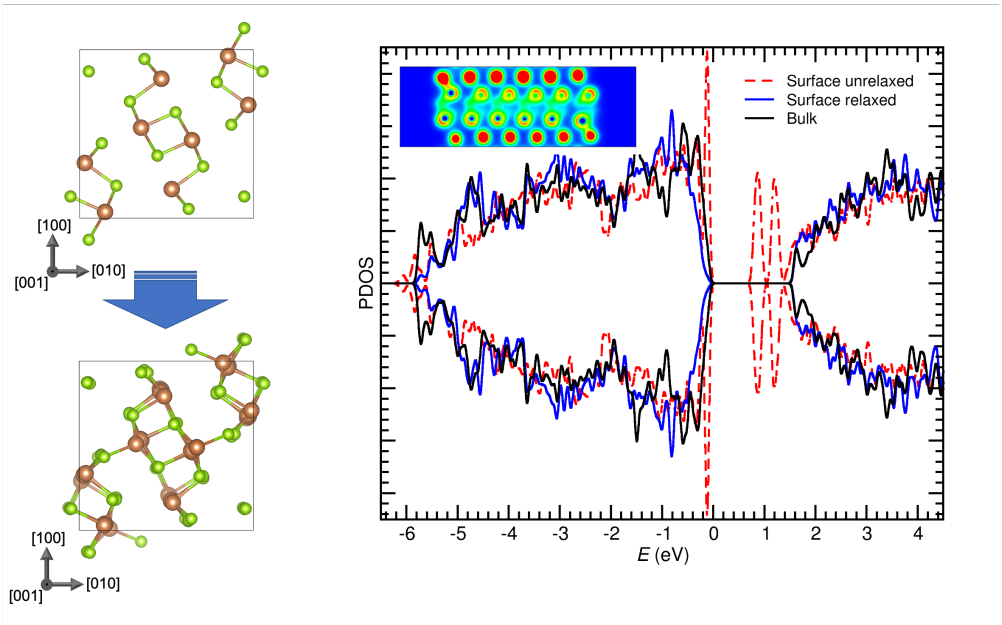

ToC Entry